Energy transfer and dissipation tensor anisotropy in atmospheric turbulence

Cabral Santos Pestana, Tiago; Thalhammer, Matthias; Hickel, Stefan

Publication date
2018

Document Version
Accepted author manuscript

Published in
Proceedings of the ERCOFTAC Symposium on Engineering Turbulence Modelling and Measurement (ETMM12)

ENERGY TRANSFER AND DISSIPATION TENSOR ANISOTROPY IN ATMOSPHERIC TURBULENCE

T. Pestana[1], *M.Thalhammer*[1] *and S. Hickel*[1]

[1] *Aerodynamics Group, Faculty of Aerospace Engineering, Technische Universiteit Delft, Kluyverweg 1, 2629 HS Delft, The Netherlands*

t.pestana@tudelft.nl

1 Introduction

Turbulence in the atmosphere is generally affected by rotation and stratification. The combination of these two effects endows the atmosphere with wave-like motions, which are particularly relevant for the mixing processes in the middle and upper atmosphere. Gravity-waves, for instance, can transfer energy over large distances, carrying energy from where they are created to regions thousands of kilometers away (Fritts and Alexander (2003)). Due to wave instabilities, they break and induce small scale turbulence in the overall large scale flow, thus contributing to the mixing process. In current general circulation models, however, small scale motion is not resolved and instead only parametrized. Hence, understanding the breaking process can potentially lead to improved parametrization models and predictions.

Depending on their frequency, gravity-waves can be classified as high-frequency gravity-waves (HGWs) and low-frequency inertia-gravity waves (IGWs). The breaking behavior of IGWs differs fundamentally from HGWs and must be investigated separately (Dunkerton (1997), Achatz and Schmitz (2006), Fruman et al. (2014)). Given that the wave breaking event leads to small scale three-dimensional turbulence, computational investigations must resolve a very large range of dynamic scales of motions (Lelong and Dunkerton (1998) and Fritts et al. (1994)). For HGWs, three-dimensional high resolution Direct Numerical Simulations (DNS) have already been performed, for example, by Fritts et al. (2009) and Remmler et al. (2015). For IGWs, fully three-dimensional investigations of a IGW breaking in the upper mesosphere were first presented by Remmler et al. (2012) and Fruman et al. (2014).

The present work focuses on turbulence induced by the breaking events of IGWs. We extend the work of Remmler et al. (2012) and Fruman et al. (2014) by performing DNS of an IGW breaking at a lower altitude and correspondingly higher Reynolds number typical of the middle mesosphere. Additionally, we explain the turbulent energy transfer during breaking events and analyze the structure of the turbulence dissipation tensor. Finally, we perform Large-Eddy Simulations (LES) using different models. We compare LES results to our DNS and asses if these models can be used to qualitatively predict breaking events.

2 Methodology

We initially perform three-dimensional DNS of an inertia-gravity wave breaking in the atmosphere at a geopotential altitude of 72 km (middle mesosphere) and 81 km (upper mesosphere) in the US standard atmosphere. The Reynolds numbers based on the wavelength and velocity amplitude are 43 860 (81 km, $\nu = 1$ m^2/s) and 174 720 (72 km, $\nu = 0.25$ m^2/s). We solve the incompressible Navier-Stokes equations on a f-plane together with a transport equation for the buoyancy field (Boussinesq approximation) in a triple periodic domain aligned with the wave. The governing equations in vector notation read:

$$\nabla \cdot \mathbf{u} = 0 \tag{1}$$

$$\mathbf{u} \cdot \nabla \mathbf{u} = -\nabla p + b\mathbf{n} - f_c \mathbf{n} \times \mathbf{u} + \nu \nabla^2 \mathbf{u} \tag{2}$$

$$\frac{\partial b}{\partial t} + \mathbf{u} \cdot \nabla b = -\mathbf{u} \cdot N^2 \mathbf{n} + \alpha \nabla^2 b. \tag{3}$$

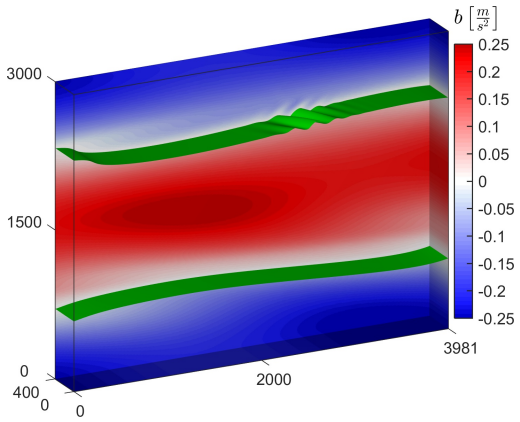

Figure 1: Initial condition for the IGW breaking simulations. Monochromatic base wave disturbed by its leading transverse normal mode and its fastest growing singular vector. Contours of the buoyancy field and an iso-surface at $b = 0$ are also shown.

Here $\mathbf{u}$ is the velocity field, p denotes pressure, ν is the kinematic viscosity, α the thermal diffusivity and b the buoyancy field. Additionally, $f_c = 2\Omega_E \sin(\phi_E)$ is the Coriolis parameter, in which Ω_E is the Earth's angular velocity and ϕ_E is the latitude on the f-plane, N is the Brunt-Väisälä frequency and $\mathbf{n}$ is a unity-vector in the direction of gravitational acceleration. As a numerical scheme, we employ a pseudo-spectral method for representing the spatial gradients, Rogallo's integrating factor for exact integration of the Coriolis and viscous terms and a third-order Runge-Kutta scheme for time-integration of the remaining terms.

The initial condition for the inertia-gravity wave breaking simulations correspond to a base wave superimposed with a primary and secondary perturbation. While the base wave is a statically unstable monochromatic IGW, the primary perturbation is its leading normal mode (NM) and the secondary perturbation is its fastest growing singular vector (SV). The initial conditions were constructed and provided by Remmler et al. (2013) following the methodology proposed in Fruman and Achatz (2011). For illustration, the initial buoyancy field is presented in Fig. 1. The monochromatic IGW varies in the z-direction with a wavelength of 3000 m, the NM superimposed onto the IGW varies in the x-direction with a wavelength of 3981 m and the SV in the upper half of the IGW with a wavelength of 400 m. These determine the domain size in all three directions, i.e. $\mathcal{L}_x = 3981$ m, $\mathcal{L}_y = 400$ m and $\mathcal{L}_z = 3000$ m. The Direct Numerical Simulations are carried out with $1536 \times 164 \times 1152$ grid points for the 81 km case and $2048 \times 196 \times 1536$ for the 72 km case. These lead to grid sizes of around 2.5 and 2.0 m, respectively, in all three spatial directions.

For the LES, the governing equations are obtained after a spatial filter is applied to Eqs. (1) to (3). The filtering operation introduces unknowns to the system, which are related to subgrid quantities. From Eq. (2), filtering leads to the subgrid stresses $\tau_{ij} = \widetilde{u_i u_j} - \widetilde{u}_i \widetilde{u}_j$, and, from Eq. (3), we have the subgrid scalar flux vector $h_i = \widetilde{u_i b} - \widetilde{u}_i \widetilde{b}$ (tilde denotes filtered quantities).

To close the subgrid stresses, we employ two different models. The first one is the classic dynamic Smagorinsky model (DSM), in which the deviatoric part of the subgrid stresses are assumed to be linearly related to the filtered strain-rate tensor, $\widetilde{S}_{ij}$, i.e

$$\tau_{ij}^d = -2\nu_T \widetilde{S}_{ij}. \tag{4}$$

The eddy viscosity ν_T is modeled as

$$\nu_T = (C_S \Delta)^2 (\widetilde{S}_{ij} \widetilde{S}_{ij})^{1/2}, \tag{5}$$

and a dynamic procedure based on Germano's identity is used to determine the model constant C_S. The second model is an Explicit Algebraic Subgrid Stress Model (EASSM), similar to the one of Marstorp et al. (2009). Within this approach, the subgrid stresses are

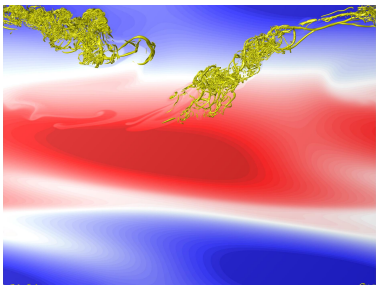

(a) t = 0.10 h

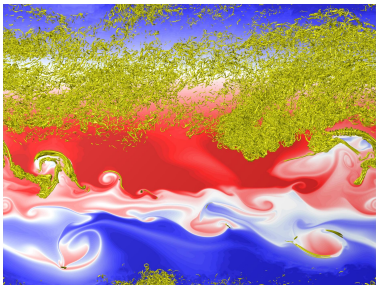

(b) t = 0.33 h

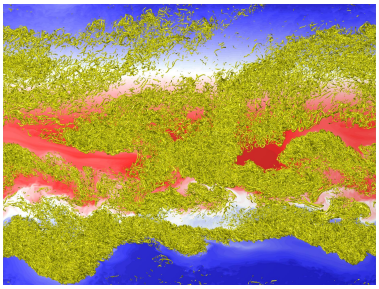

(c) t = 0.42 h

Figure 2: Time series of the first breaking event. Isosurfaces of $Q = 0.03\,\mathrm{s}^2$ with contours of buoyancy b in the x-z plane at $y = 400$ m.

projected on a tensorial basis, i.e.

$$\tau_{ij}^d = k_{sgs} \sum_{k=1}^{2} G^{(k)} T_{ij}^{(k)}, \tag{6}$$

where $G^{(k)}$ are coefficients and $T_{ij}^{(k)}$ are the basis tensors (see Pope (1975)). Determination of the coefficients $G^{(k)}$ follow from the evolution equations for τ_{ij}^d together with the weak-equilibrium assumption. In the original model of Marstorp et al. (2009), it is assumed that the production term is in balance with the kinetic energy dissipation rate. In our version, however, we relax this assumption by considering instead that their ratio varies slowly in time. Additionally, to close Eq. (6), we use an evolution equation for the subgrid kinetic energy k_{sgs}.

For the subgrid scalar flux, in combination with the DSM, we employ an eddy diffusivity model (EDM) with constant Prandtl number ($Pr_T = 0.4$):

$$h_{ij} = -\frac{\nu_T}{Pr_T} \frac{\partial \widetilde{b}}{\partial x_i}. \tag{7}$$

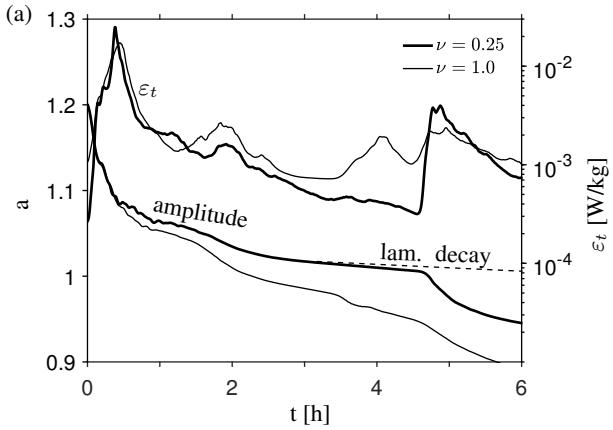

Figure 3: Temporal development of the total dissipation ε_t and the non-dimensional amplitude a. Dashed line indicates a laminar decay of the amplitude.

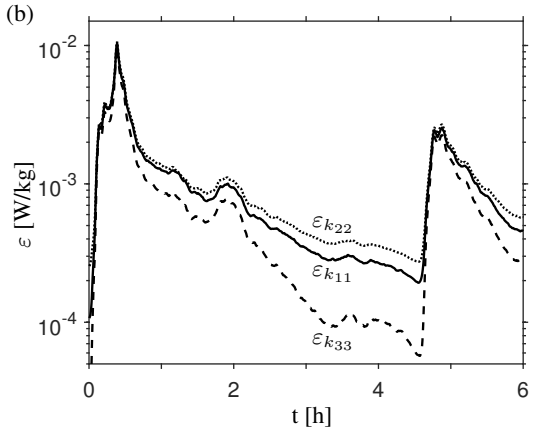

Figure 4: Diagonal components of the Reynolds stress dissipation rate tensor.

With the EASSM, we use a dynamic EDM (DEDM), in which Pr_T is determined dynamically (Moin et al. (1991)).

The LES are performed in physical space using a finite-volume solver on $128 \times 32 \times 96$ grid points. The numerical scheme is based on a fourth-order central difference scheme to approximate the spatial derivatives and time integration is achieved by a standard third-order Runge-Kutta scheme. (Remmler et al. (2015)).

3 Results

Breaking events are characterized by a sharp increase in the energy dissipation rate, which is triggered by the surge of turbulent flow structures. Figure 2 shows contours of the buoyancy field together with coherent turbulent structures visualized by isosurfaces of the Q-criterion during the primary breaking event of the 72 km case. Three-dimensional structures develop from the initial disturbance of the wave (Fig. 2a). We observe that these structures are continuously transported horizontally, spread primarily over the upper half part of the domain (Fig. 2b), and eventually occupy the entire domain (Fig. 2c). As observed by Remmler et al. (2013), the breaking events are also followed by an increase in energy dissipation, which mainly stems from mixing in the lower half of the domain. From Fig. 2, we can infer that the isopycnals in the upper half are almost horizontally aligned and the different buoyancy layers are therefore neatly separated from each other, while the lower half shows regions of intense mixing and consequently higher gradients. Turbulence is not omnipresent in the domain but rather confined to regions where the wave breaks.

Figure 3 presents the base wave amplitude nondimensionalized by the static stability limit. For the first 30 minutes, the projection onto the non-dimensional amplitude a follows the same trend for both cases. However, for $t > 0.5$ h, the amplitude decay rate of the lower altitude case slows down almost to the laminar rate until the wave breaks again —when the Prandtl number is unity, a unperturbed laminar wave decays with $a(t) = a \cdot e^{-\nu k^2 t}$ (Fruman et al. (2014)). This is an interesting observation since the non-dimensional amplitude is still above the threshold of static instability ($a = 1$) after the first breaking event.

The time evolution of the total dissipation in Fig. 3 shows four distinguishable peaks for the higher altitude case and two peaks for the lower altitude case. Splitting the total energy dissipation rate into its kinetic and potential contributions (not shown), reveals that the kinetic energy dissipation rate is the main source of dissipation. Therefore, the peak events observed in Fig. 3 are due to small scales in the velocity rather than in the buoyancy field. During the first breaking event, the total dissipation evolves similarly for both altitudes, what we attribute to the well defined initial conditions that force the wave to break almost immediately. After the first breaking event, both cases show a trend towards lower dissipation levels until the second breaking event takes place and dissipation increases again.

Figure 4 shows the diagonal elements of the kinetic energy dissipation rate $\varepsilon_k = (\varepsilon_{k11} + \varepsilon_{k22} + \varepsilon_{k33})/2$ for the higher Reynolds case. The dissipation tensor is highly isotropic during the first and second breaking event, whereas in-between these events we observe a strongly anisotropic tensor. The same analysis has been carried out for the higher altitude case, with simulations showing the same tendency towards isotropic dissipation during breaking events. Nevertheless, at higher altitudes and therefore lower Reynolds numbers, the degree of anisotropy in-between the breaking events is much more pronounced. We attribute the tendency towards isotropy to the strong mixing induced by the wave breaking process and the anisotropic decay to stratification effects.

Figure 5 shows the compensated spectral energy

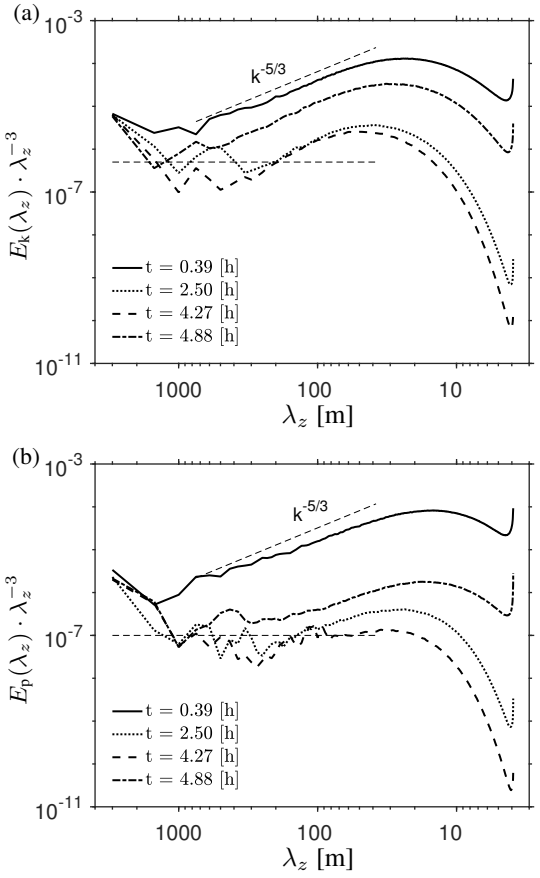

Figure 5: Compensated spectral energy density plotted over the vertical wavelength at different instants of time. (a): kinetic energy E_k; (b): potential energy E_p

density for the kinetic (Fig. 5a) and potential energy (Fig. 5b) plotted over the vertical wavelength λ_z. Two spectra are at the time of peak dissipation, t $= 0.39$ h and t $= 4.88$ h and the other two are at calmer periods, t $= 2.50$ h and t $= 4.27$ h, for the 72 km case. During the breaking event, we see a $\lambda_z^{-5/3}$ power-law over a wide range of wavelengths, whereas at calmer periods, our data agrees best with a λ_z^{-3} scaling law. These results suggest that the influence of stratification is weak during the breaking events and that it gains importance the calmer the flow field becomes.

Regarding the energy distribution during breaking events, the Reynolds stress tensor shows that most of the kinetic energy is contained in the $\langle uu\rangle$ and $\langle vv\rangle$ components. Following their evolution over time, we see that during breaking events energy is not only transfered from these terms to $\langle ww\rangle$, but also converted into potential energy, which is stored as $\langle bb\rangle/N^2$. With respect to the off-diagonal elements, the $\langle uv\rangle$ correlation is mostly positive but undergoes a sign change during the second breaking event, whereas $\langle uw\rangle$ is slightly negative throughout the whole simulation; $\langle vw\rangle$ on the other hand, fluctuates weakly around zero.

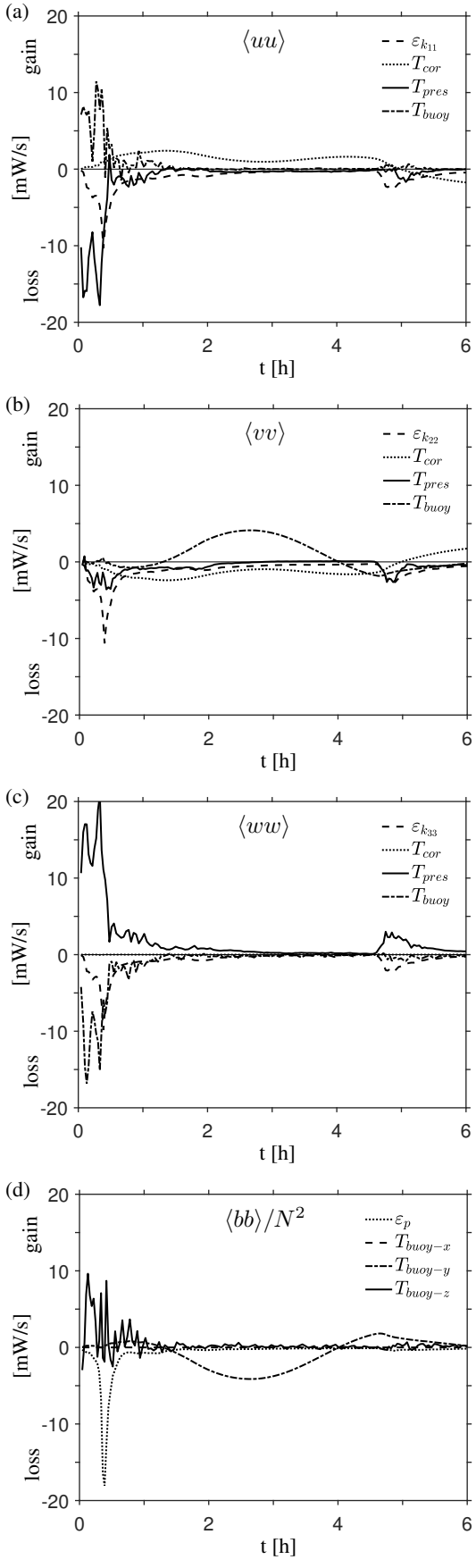

Figure 6: Term-by-term kinetic and potential energy budget.

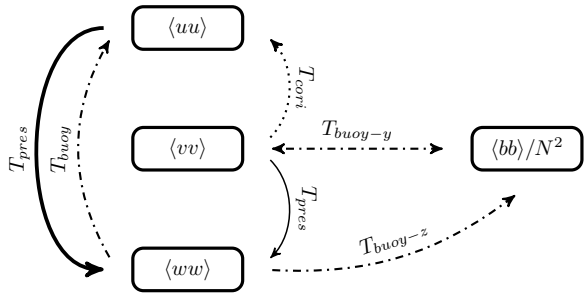

Figure 7: Schematic of the energy transfer mechanism and the role of each term during the wave breaking event. Line styles follow Fig. 6. Difference in the line thickness for the pressure term indicates the strength of the transport.

To detail the energy transfer process, we present a kinetic and potential energy budget analysis. The evolution equations for the kinetic and potential energy are (no summation implied)

$$\partial_t E_{k,ii} = -T_{cor,ii} + T_{adv,ii} + T_{pres,ii} + T_{buoy,ii} - \varepsilon_{k,ii} \tag{8}$$

and

$$\partial_t E_p = T_{adv} - T_{buoy-x} - T_{buoy-y} - T_{buoy-z} - \varepsilon_p \,, \tag{9}$$

where the terms on the right-hand side of Eqs. (8) and (9) represent the contributions due to Coriolis force, advection, pressure, buoyancy and dissipation. The term-by-term energy budget of Eqs. (8) and (9) is presented in Fig. 6 for the components of the kinetic energy (a)-(c) and the potential energy (d).

From Fig. 6 we see that during breaking events the main energy supplier to the third component $\langle ww \rangle$ is $\langle uu \rangle$ through the pressure transport term T_{pres}. As the first perturbation due to the leading normal mode is in x-direction, we attribute the energy transfer from $\langle uu \rangle$ to $\langle ww \rangle$ to the roll-up prior to the breaking of the wave. We also observe that $\langle uu \rangle$ transfers energy to $\langle vv \rangle$, but this process is much weaker. Acting as the main coupling term between the potential and kinetic energy, T_{buoy-z} converts part of the energy gained by $\langle ww \rangle$ into potential energy. The remaining energy in $\langle ww \rangle$ is then either transferred back to $\langle uu \rangle$ or dissipated. The Coriolis term T_{cor}, on the other hand, is responsible for the transport of energy between $\langle vv \rangle$ and $\langle uu \rangle$. The direction of energy transfer, however, is related to the sign of the $\langle uv \rangle$ correlation: for positive $\langle uv \rangle$, the energy flows from $\langle vv \rangle$ to $\langle uu \rangle$ and for negative $\langle uv \rangle$, vice-versa. Finally, the distinct energy gain by $\langle vv \rangle$ for $1.5 < t < 4$ h is found to be due to the buoyancy transport term T_{buoy-y}. The entire transfer mechanism and the role of each term is summarized in Fig. 7.

Now we move our focus to LES and asses the performance of DSM-EDM and EASSM-DEDM in predicting breaking events. Fig. 8 shows the total energy

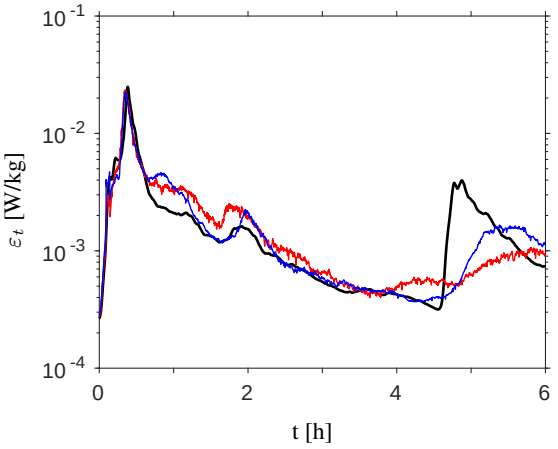

Figure 8: Temporal development of the total dissipation ε_t. Line colors for different sources of data: DNS (black); DSM-EDM (red); EASSM-DEDM (blue).

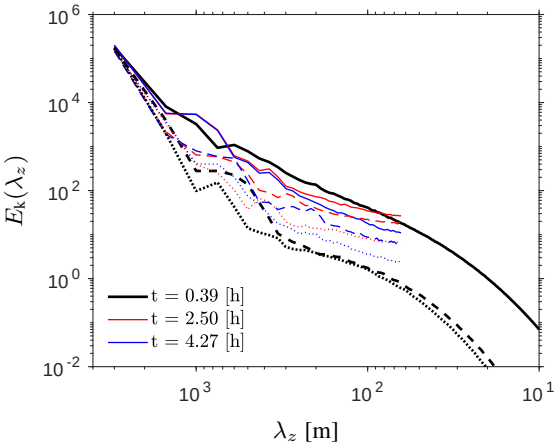

Figure 9: Spectral energy density plotted over the vertical wavelength at different instants of time. Line colors as in Fig. 8

dissipation rate, as the wave evolves in time. By comparing results with the reference data, we see that both LES models successfully represent the first breaking event. A peak of dissipation corresponding to the second breaking event is also reproduced with both LES models. However, the instant of time at which it occurs is better captured by the EASSM-DEDM model. With respect to the last breaking event, both models predict it only marginally, with the EASSM-DEDM indicating a stronger peak of ε_k.

In Fig. 9 we present the one-dimensional energy spectrum at three time instants and we find that neither of the models can accurately reproduce the energy level at smaller wavelengths. A qualitative comparison, however, shows that EASSM-DEDM delivers a better prediction for the slope of the energy spectrum, as the spectra from EASSM-DEDM is roughly parallel to the ones from the DNS data. The DSM-EDM,

on the other hand, shows an accumulation of energy at small wavelengths, which ultimately leads to a wrong power-law.

4 Conclusions

We presented results from fully resolved three-dimensional simulations of inertia-gravity wave breaking at two geopotential altitudes of 72 km and 81 km. Time evolution of the kinetic energy dissipation tensor revealed a trend towards isotropy during the breaking events, which was attributed to the strong mixing induced by the wave breaking process. At calmer periods, i.e. in-between breaking events, the kinetic energy dissipation tensor is strongly anisotropic. Accordingly, the vertical energy spectra showed a $\lambda_z^{-5/3}$ power-law at the peak of dissipation, and λ_z^{-3} at calmer periods. For the lower Reynolds number case we observed that both spectra behave in a similar fashion. A term-by-term energy budget analysis for both the kinetic and potential energy was also presented and the role of each term was explained and summarized in form of a diagram. Last, we discussed LES results obtained with a dynamic Smagorinsky model (DSM) and an Explicit Algebraic Subgrid Stress model (EASSM). We obtained slightly better results with the EASMM for the structure of breaking events and turbulence energy spectra.

References

Achatz, U. and Schmitz, G. (2006), Shear and Static Instability of InertiaGravity Wave Packets: Short- Term Modal and Nonmodal Growth, *J. Atmospheric Sci.*, Vol. 63, pp. 397-413.

Dunkerton, T.J. (1997), Shear Instability of Internal Inertia-Gravity Waves, *J. Atmospheric Sci.*, Vol. 54, pp. 1628-1641.

Fritts, D.C. and Alexander, M.J. (2003), Gravity wave dynamics and effects in the middle atmosphere, *Rev. Geophys.*, Vol. 41 , pp. 1003.

Fritts, D.C., Isler, J. R. and Oyvind, A. (1994), Gravity wave breaking in two and three dimensions structure, *J. Geophys. Res*, Vol. 99, pp. 8095-8108.

Fritts, D.C., Wang, L., Werne, J., Lund, T. and Wan, K. (2009), Gravity Wave Instability Dynamics at High Reynolds Numbers Part I and II, *J. Atmospheric Sci.*, Vol. 66, pp. 1149-1171.

Fruman, M.D. and Achatz, U. (2011), Secondary Instabilities in Breaking InertiaGravity Waves, *J. Atmospheric Sci.*, Vol. 69, pp. 303322.

Fruman, M.D., Remmler, S., Achatz, U. and Hickel, S. (2014), On the construction of a direct numerical simulation of a breaking inertia-gravity wave in the upper mesosphere, *J. Geophys. Res*, Vol. 119 ,pp. 1161311640.

Lelong, M.P. and Dunkerton, T.J. (1998), InertiaGravity Wave Breaking in Three Dimensions. Parts I and II, *J. Atmospheric Sci.*, Vol. 55, pp. 24732501.

Marstorp, L., Brethouwer, G., Grundestam, O., Johansson, A. V. (2009) Explicit algebraic subgrid stress models with application to rotating channel flow, *J. Fluid Mech.*, Vol. 639, pp. 403-432

Moin, P., Squires, K., Cabot, W., Lee, S. (1991) A dynamic subgrid-scale model for compressible turbulence and scalar transport, *Phys. Fluids*, Vol. 3, pp. 2746-2757

Remmler, S., Hickel, S., Fruman, M.D. and Achatz, U. (2015), Validation of Large-Eddy Simulation Methods for Gravity Wave Breaking, *J. Atmospheric Sci.* Vol 72, pp. 35373562.

Remmler, S., Fruman, M.D. and Hickel, S. (2013), Direct numerical simulation of a breaking inertiagravity wave, *J. Fluid Mech.*, Vol. 722, pp. 424436.

Remmler, S. and Hickel, S. (2012), Spectral structure of stratified turbulence: Direct numerical simulations and predictions by large eddy simulation, *Theor. Comput. Fluid Dyn.*, Vol. 27, pp. 319-336